npj | 2D materials and applications

www.nature.com/npj2dmaterials

ARTICLE OPEN

Check for updates

# Main-group metal elements as promising active centers for single-atom catalyst toward nitric oxide reduction reaction

Qian Wu[1], Baibiao Huang[1], Ying Dai[1]✉, Thomas Heine[2,3,4]✉ and Yandong Ma[1]✉

Current research efforts on single-atom catalysts (SACs) exclusively focus on nonmetal or transition-metal atoms as active centers, while employing main-group metal elements is seemingly excluded because their delocalized s/p-bands are prone to yield a broadened resonance for the interaction with adsorbates. Here, we use high-throughput first-principles calculations to investigate the possible incorporation of Mg, Al, and Ga to form graphene-based SACs for NO reduction reaction (NORR) toward $NH_3$. 51 SAC candidates with different metal coordination environments have been computationally screened employing a rationally designed four-step process, yielding six SACs with high catalytic activity and NORR selectivity. The performance is rationalized by the modulation of s/p-band filling of the main-group metals. The adsorption free energy of NO is identified as an efficient descriptor for such SACs. The underlying physical mechanism is revealed and generally applicable to other main group metal SACs. These fundamental insights extend NORR SACs to main-group metal elements.

*npj 2D Materials and Applications* (2022)6:52 ; https://doi.org/10.1038/s41699-022-00326-4

## INTRODUCTION

Single-atom catalysts (SACs) have drawn increasingly intense attention in electrocatalysis, as they have great potential to provide unmatched high activity and selectivity for multiple chemical reactions[1–3]. The catalytic activity of SAC active centers is strongly correlated to their coordination environment[4–7]. In recent years, much progress has been made, and various SACs have been developed both theoretically[8–11] and experimentally[12–15]. The catalytic properties of some theoretically predicted SACs have been verified experimentally[16–18]. Nonetheless, these investigations mostly focus on nonmetal or transition-metal atoms as SAC active centers[19]. While the catalytic activity of the nonmetal SACs is caused by hybridized s-p orbitals, transition-metal SACs benefit from the localized character of d orbitals[20–23]. The introduction of elements besides nonmetal and transition-metal atoms as SAC active centers remains to be explored.

In contrast to transition metals, main-group metal elements such as Mg, Al, and Ga, generally exhibit a delocalized s/p-band, which is prone to broaden the adsorbate states[22,24,25]. Such interaction is thought to yield either too strong or too weak adsorption for adsorbates. This would poison active centers or fail to activate adsorbates, which thus seemingly excludes any possibility to achieve high-performing SACs based on main-group metal elements[25]. Nevertheless, recently main-group metal elements have been employed as co-electrocatalysts in dual atomic catalysis, where they act as promising separators and facilitate the electroactivity of the connected transition-metal atoms[19]. Moreover, Mg ion that is contained in enzymes has been proven to show a suitable affinity for oxygenated species[26–29]. These observations suggest that, despite the unbefitting delocalized s/p-band, main-group metal elements might still offer the potential to be active centers in SACs.

Among various electrocatalysis reactions, the direct electrochemical NO reduction reaction (NORR) toward $NH_3$ receives special attention as it combines both NO removal and $NH_3$ synthesis[30–33]. For NO removal, the conventional technology is based on selective catalytic reduction, which consumes valuable $NH_3$ or $H_2$[34,35]. The alternative, electrochemical $NH_3$ synthesis from $N_2$, suffers from low reaction rate and Faradaic efficiency[36–39]. Undoubtedly, a successful realization of NORR, converting NO into $NH_3$ directly, will be a breakthrough[20,30,40]. Though highly valuable, the direct NO-to-$NH_3$ conversion is essentially unexplored, and only a few NORR electrocatalysts have been reported to date[30–33,40,41]. Exploring suitable NORR catalysts thus is of great economic interest and scientific importance, but a formidable task.

In this work, we systematically investigate the possibility of introducing main group metal elements (i.e., Mg, Al, and Ga) to form graphene-based SACs and investigate their suitability to drive the NORR. In strong contrast to expectations, i.e., that suitable active centers are either nonmetal or transition-metal atoms, we demonstrate that indeed main-group metal elements can serve as promising active centers for SACs toward NORR. Through high-throughput screening based on first-principles calculations, six SAC systems out of 51 candidates have been selected as they exhibit superior catalytic activity and selectivity for NORR toward $NH_3$. Importantly, the NORR process can occur spontaneously in these systems. The excellent performances of these systems are closely related to the modulation of s/p-band filling of the main-group metal centers derived from regulating the coordination environment. A rational and generally applicable four-step screening principle is mapped out. Furthermore, we discover that the adsorption free energy of NO is an efficient catalytic descriptor for such SACs. Our findings provide an effective guidance for understanding the potential introduction of main-group metal elements in SACs, and shed light on the further development of NORR catalysts.

[1]School of Physics, State Key Laboratory of Crystal Materials, Shandong University, Shandanan Str. 27, 250100 Jinan, China. [2]TU Dresden Fakultät für Chemie und Lebensmittelchemie, Bergstraße 66c, 01062 Dresden, Germany. [3]Helmholtz-Zentrum Dresden-Rossendorf, Forschungsstelle Leipzig Permoserstraße 15, 04318 Leipzig, Germany. [4]Department of Chemistry, Yonsei University, Seodaemun-gu, Seoul 120-749, Republic of Korea. ✉email: daiy60@sina.com; thomas.heine@tu-dresden.de; yandong.ma@sdu.edu.cn

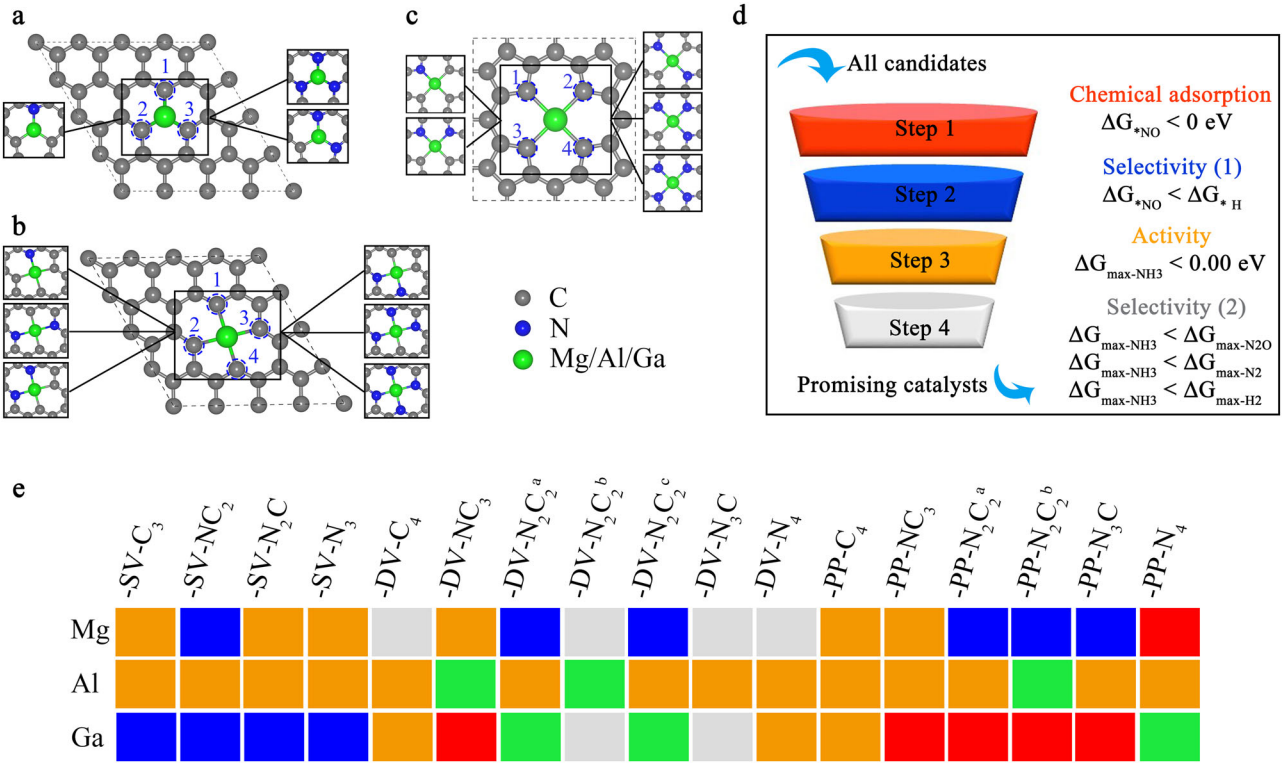


**Fig. 1 Schematic illustrations of single Mg/Al/Ga atom supported on N-doped graphene with different coordination environments and a screening strategy flowchart for NORR toward $NH_3$. a** Single vacancy site coordinated with three C/N atoms (SV-$N_{3-n}C_n$, $n = 0$–3). **b** Double vacancy site coordinated with four C/N atoms (DV-$N_{4-n}C_n$, $n = 0$–4). **c** Porphyrin site coordinated with four C/N atoms (PP-$N_{4-n}C_n$, $n = 0$–4). The unit cells are marked in dotted lines, and the solid rectangles highlight the local configurations with different numbers of N atoms. Atoms marked with dotted circles in (**a**–**c** indicate the replaceable C atoms. **d** Flowchart of the screening scheme to identify the promising SACs with main group metal active centers for NORR toward $NH_3$. **e** Color code map corresponding to the flowchart of the screening scheme shown in (**d**). The red, blue, orange and gray color codes indicate the eliminated systems from the first, second, third, and fourth screening steps, respectively, and the green color code indicates the final candidates.

## RESULTS AND DISCUSSION

### Constructing of main group metal single-atom electrocatalysts

To support the dispersed Mg/Al/Ga atoms, we have chosen N-doped graphene as a substrate in light of the following reasons. First, N-doped graphene is well defined and has been demonstrated to act as an excellent substrate for different SACs both theoretically and experimentally. It merits structural flexibility and thermostability, so it can be used in harsh chemical environments[4,5,42–46]. Second, it has different coordination modes and thus offers various coordination environments for active centers. Third, N-doped graphene exhibits excellent conductivity, facilitating fast electron transfer during electrocatalysis. Figure 1a–c illustrates the schematic configurations of single Mg/Al/Ga atom supported on graphene with the coordination of N atoms. By regulating the N-coordination, 17 configurations are constructed for each case, including four SV-$N_{3-n}C_n$, seven DV-$N_{4-n}C_n$ and six PP-$N_{4-n}C_n$ (Fig. 1a–c), which results in a total of 51 SAC candidates. By comparing the adsorption energy and the cohesive energy of the Mg/Al/Ga, our results indicate that for all the candidates, the main group metal atoms can stably anchor on the substrate (Supplementary Table 2), and the corresponding optimized crystal structures are shown in Supplementary Figs. 1–3. The previous work[43] has synthesized the configurations of Mg atom coordinated with N atom on graphene, and they also point out that all similar systems including Al and Ga can be prepared following the same method as well. The Bader charge analysis indicates that the supported main group atom donates electrons to the substrate for all these systems, as listed in Supplementary Table 3. The resultant positively charged metal atoms act as Lewis acids and hence become active sites for catalytic reactions[47–49].

### Screening of superior main group metal SACs for NORR

The electrochemical NORR for $NH_3$ synthesis is a complex process involving five hydrogenation steps, i.e., $NO + 5H^+ + 5e^- = NH_3 + H_2O$. To identify suitable NORR SACs, we design a four-step screening strategy, as schematically illustrated in Fig. 1d. First of all, the NO molecule should be chemisorbed and activated on the SAC center ($\Delta G_{*NO} < 0$, where $\Delta G_{*NO}$ is the Gibbs free energy of activated *NO adsorption), which is required to facilitate the subsequent hydrogenation process. Second, the competitive proton adsorption should be suppressed to protect the electrocatalyst from being poisoned ($\Delta G_{*NO} < \Delta G_{*H}$, where $\Delta G_{*H}$ is the Gibbs free energy change for H adsorption). Third, the criterion of $\Delta G_{max\text{-}NH3} < 0$ ($\Delta G_{max\text{-}NH3}$ is the maximum Gibbs free energy change of hydrogenation steps for $NH_3$ synthesis via the most favorable reaction mechanism) guarantees the reaction could proceed spontaneously. Finally, $\Delta G_{max\text{-}NH3} < \Delta G_{max\text{-}N2O}$, $\Delta G_{max\text{-}NH3} < \Delta G_{max\text{-}N2}$ and $\Delta G_{max\text{-}NH3} < \Delta G_{max\text{-}H2}$ ($\Delta G_{max\text{-}N2O/N2/H2}$ is the maximum Gibbs free energy change of hydrogenation steps for $N_2O/N_2/H_2$ synthesis via the corresponding most favorable reaction mechanism) are adopted to select systems of high $NH_3$ selectivity. Following this four-step screening strategy, the highly efficient NORR SACs with main-group metal elements as active centers for $NH_3$ synthesis can be identified.

For NORR process, the first reaction step is adsorption (and activation) of NO, which plays a critical role for the subsequent reactions. Given the non-equivalence between N and O atoms, three possible adsorption patterns of NO are considered,

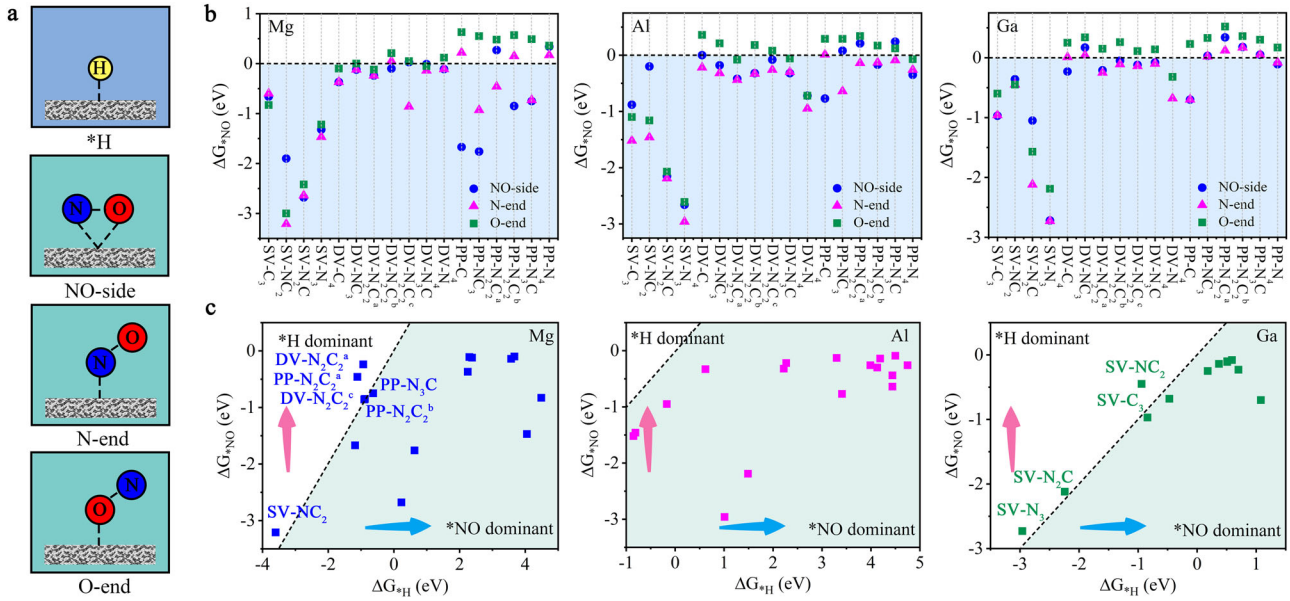


**Fig. 2 Adsorption performance of NO molecule and selectivity between the adsorptions of NO and H on SAC candidates. a** The possible adsorption patterns of H and NO (i.e., N-end, O-end and NO-side patterns). **b** Gibbs free energy changes for NO adsorption with N-end, O-end and NO-side patterns. **c** Comparison of the adsorption free energies of H proton and NO molecule with the corresponding most favorable adsorption pattern.

i.e., N-end, O-end and NO-side patterns (Fig. 2a). This gives rise to 153 adsorption configurations in total. The corresponding $\Delta G_{*NO}$ for all these configurations are shown in Fig. 2b and Supplementary Tables 4–6. Intriguingly, the N-end pattern is most preferred in energy for almost all SAC candidates, except for Mg-SV-$C_3$ (O-end) and for Mg-PP-$C_4$/-$NC_3$, Al-PP-$C_4$ and Ga-DV-$C_4$ (NO-side), see Supplementary Figs. 4–6. This behavior is expected due to the smaller electronegativity of N atom compared to O atom, making N atom more attractive to coordinate with the SAC Lewis acid site. Note that to guarantee sufficient activation of the adsorbed NO, spontaneous chemisorption of NO ($\Delta G_{*NO} < 0$) is regarded as a necessary prerequisite for NORR process. Thus, following the first screening stage, the systems shown in red color in Fig. 1e are discarded ($\Delta G_{*NO} > 0$). The other SAC candidates show negative adsorption free energies between −0.08 and −3.21 eV.

To ensure an effective chemisorption of NO, the competitive adsorption of proton should be excluded as well, which we consider by calculating the selectivity between the adsorptions of both species on the remaining SAC candidates. The Gibbs free energy changes for proton adsorption are summarized in Supplementary Table 7, and the comparison of adsorption free energies between NO and H is presented in Fig. 2c. We rule out all systems where protons are preferentially or similarly strongly adsorbed, as they would refer to proton-poisoned SAC (blue colored in Fig. 1e).

Then, we investigate the subsequent hydrogenation steps of NORR process toward $NH_3$ synthesis for the remaining 35 SAC candidates. Depending on adsorption patterns of NO, the reaction pathways of NORR toward $NH_3$ can follow the A/B-distal, A/B/C-alternating, A/B-enzymatic and C-O/N distal mechanisms (Fig. 3a). Remember that the NO adsorption patterns are O-end for Mg-SV-$C_3$ and NO-side for Mg-PP-$C_4$/$NC_3$, Al-PP-$C_4$ and Ga-DV-$C_4$, the B-distal/alternating/enzymatic and C-O distal/alternating/N-distal mechanisms are considered for them, respectively. While for the other systems, as the adsorption pattern is N-end, the A-distal/alternating/enzymatic mechanisms are explored. Also, the corresponding mixed mechanisms shown in Fig. 3a are investigated for all these systems. To determine the most favorable reaction mechanism for the NORR process, we comprehensively calculate the Gibbs free energies of all the possible reaction intermediates. And we plot the $\Delta G_{max\text{-}NH3}$ in Fig. 3c. Here, we set $\Delta G_{max\text{-}NH3} < 0$ as strict screening criterion, so the reaction can proceed spontaneously. As shown in Fig. 3c, the systems depicted in orange in Fig. 1e are eliminated. We wish to emphasize that although Mg-DV-$NC_3$, Mg-PP-$NC_3$, Al-DV-$C_4$/-$N_2C_2^a$/-$N_2C_2^c$/-DV-$N_3C$/-$N_4$, Al-PP-$N_2C_2^a$/-$N_3C$/$N_4$, and Ga-DV-$C_4$ are excluded here, they exhibit low limiting-potentials with $0.0 < \Delta G_{max\text{-}NH3} < 0.5$ eV. For the remaining 12 SAC candidates (shown in gray and green colors in Fig. 1e), the NORR process occurs spontaneously. It should be noted that these candidates with high activity are all based on DV-$N_{4-n}C_n$ or PP-$N_{4\text{-}n}C_n$ cases, while SV-$N_{3-n}C_n$ is completely excluded.

To inspect the selectivity of NORR toward $NH_3$ synthesis for the remaining 12 SAC candidates, we further investigate the possible formation of byproducts $N_2O$ and $N_2$ during the NORR process. The reaction mechanisms of NORR toward $N_2O$ and $N_2$ are illustrated in Fig. 3b. For both byproducts, the precondition is the stable adsorption of NO-dimer on the active centers[20,50]. We therefore first study the adsorption free energy of NO-dimer by considering different adsorption configurations. As shown in Supplementary Fig. 7a, the configuration with both NO featuring N-end pattern is found to be most stable for all the systems. For Ga-DV-$N_2C_2^a$ and Ga-PP-$C_4$, the positive adsorption free energy of NO-dimer prevents the formation of byproducts and suggest their high selectivity for NORR toward $NH_3$. Except these two cases, other ten systems exhibit a negative adsorption free energy of NO-dimer, and we thus further study the subsequent hydrogenation steps of NORR toward $N_2O$ and $N_2$ for the remaining ten SAC candidates following the reaction pathways shown Fig. 3b. Supplementary Fig. 7b, c lists the $\Delta G_{max}$ of hydrogenation steps for NORR toward $N_2O$ and $N_2$ via the corresponding most favorable reaction mechanisms. To show the selectivity of NORR directly, $\Delta G_{max\text{-}NH3}$ vs. $\Delta G_{max\text{-}N2O}$ and $\Delta G_{max\text{-}NH3}$ vs. $\Delta G_{max\text{-}N2}$ for the ten SAC candidates are plotted in Fig. 4a, b. It can be seen that the systems shown in gray color in Fig. 1e display $\Delta G_{max\text{-}NH3} > \Delta G_{max\text{-}N2O}/\Delta G_{max\text{-}N2}$, rendering their poor selectivity of NORR toward $NH_3$ synthesis and thus their elimination. On the other hand, the systems shown in green color in Fig. 1e exhibit $\Delta G_{max\text{-}NH3} < \Delta G_{max\text{-}N2O}/\Delta G_{max\text{-}N2}$

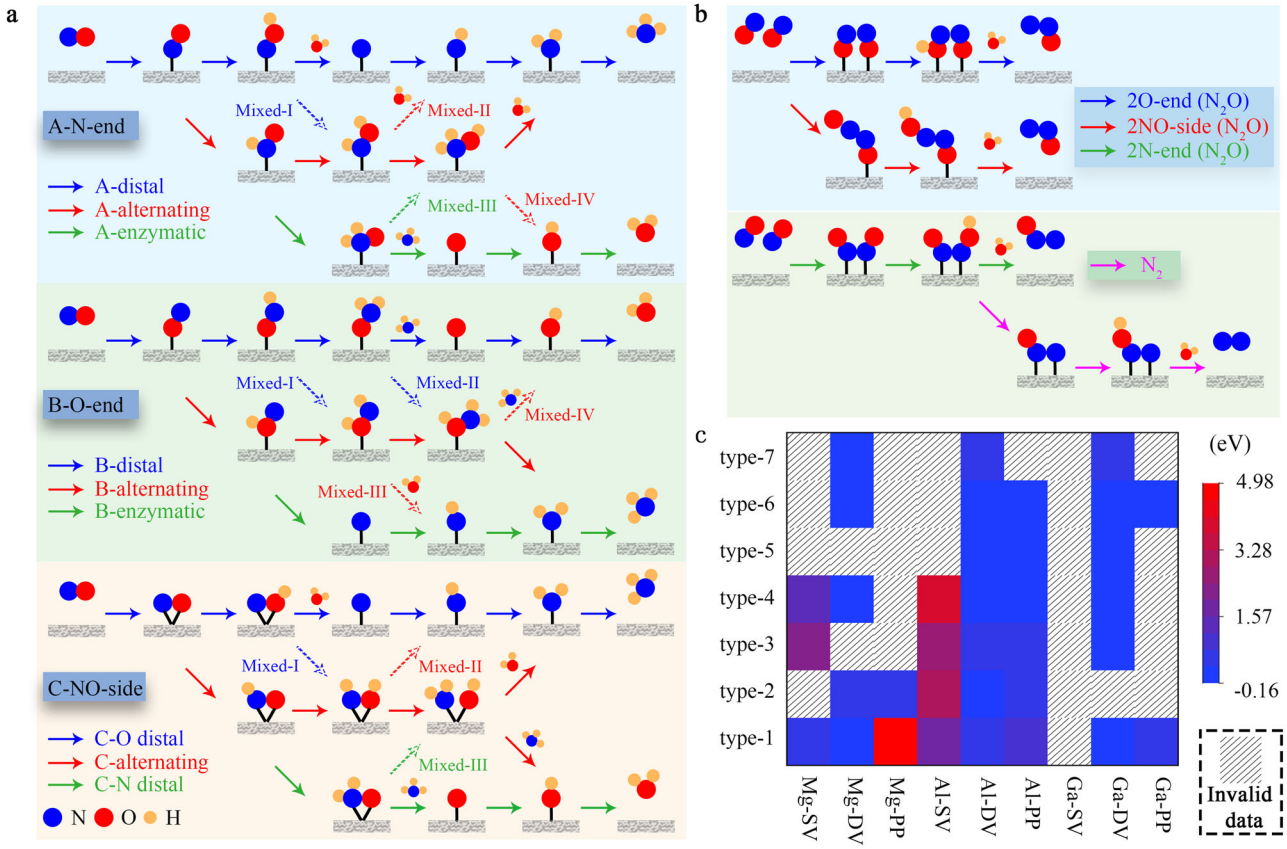


**Fig. 3 Reaction mechanism and electrocatalytic activity of NORR on SAC candidates. a** Schematic depiction of possible NORR pathways toward $NH_3$ synthesis. **b** Schematic depiction of possible NORR pathways toward $N_2O$ and $N_2$ synthesis. **c** $\Delta G_{max\text{-}NH3}$ on the remaining 35 SAC candidates via the corresponding most favorable reaction pathways. Type 1 to 6 in (**c**) is defined in Supplementary Figs. 1–6.

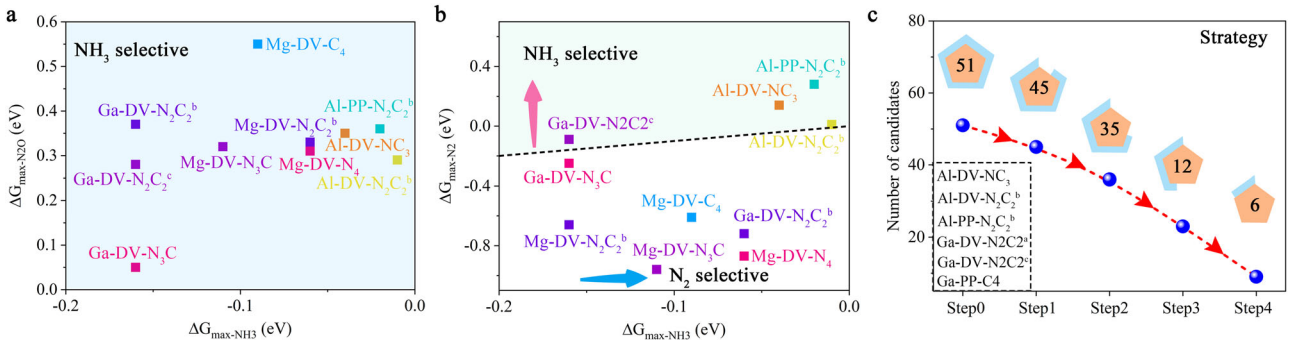


**Fig. 4 Electrocatalytic selectivity and summary of the screening strategy for NORR toward $NH_3$. a** $\Delta G_{max\text{-}NH3}$ vs $\Delta G_{max\text{-}N2O}$. **b** $\Delta G_{max\text{-}NH3}$ vs $\Delta G_{max\text{-}N2}$. **c** Illustration of the screening strategy applied to identify high-efficient electrocatalysts for NORR. Insets in (**c**) show the corresponding selected high-efficient SAC catalysts.

presenting high selectivity for NORR toward $NH_3$ synthesis. In addition to byproducts $N_2O$ and $N_2$ during NORR process, $H_2$ resulted from hydrogen evolution reaction (HER) is another byproduct that should be suppressed for improving the Faraday efficiency[20,30]. We therefore estimate the competition between NORR toward $NH_3$ and HER for these six candidates. Supplementary Fig. 8a shows the calculated $\Delta G_{*H}$ under the limiting potential of NORR toward $NH_3$ ($U_{L\text{-}NH3} = -\Delta G_{max\text{-}NH3}$), and $\Delta G_{max\text{-}NH3}$ vs $\Delta G_{*H}$ is summarized in Supplementary Fig. 8b. HER process is significantly suppressed for all these six candidates, ensuring the excellent selectivity of NORR for $NH_3$. This combined with their high NORR activity makes these six systems (Figs. 1c, 4c) very promising SACs for NORR toward $NH_3$. Their corresponding free energy diagrams and the optimized intermediates of these screened SACs during the NORR toward $NH_3$ are shown in Supplementary Fig. 9 and Supplementary Fig. 10 shows the electronic properties of these six SACs. While Al-DV-$NC_3$ is a semiconductor with indirect band gap of 0.70 eV, the other five systems are metallic with states of both spin polarizations crossing the Fermi level. Therefore, all these six SACs harbor high conductivity, facilitating fast electron transfer during the reaction process.

While the thermodynamic analyses indicate Al-DV-$NC_3$, Al-DV-$N_2C_2^b$, Al-PP-$N_2C_2^b$, Ga-DV-$N_2C_2^a$, Ga-DV-$N_2C_2^c$, and Ga-PP-$N_4$ are promising NORR electrocatalyst candidates, it is also important to investigate the kinetic barriers of the most thermodynamically

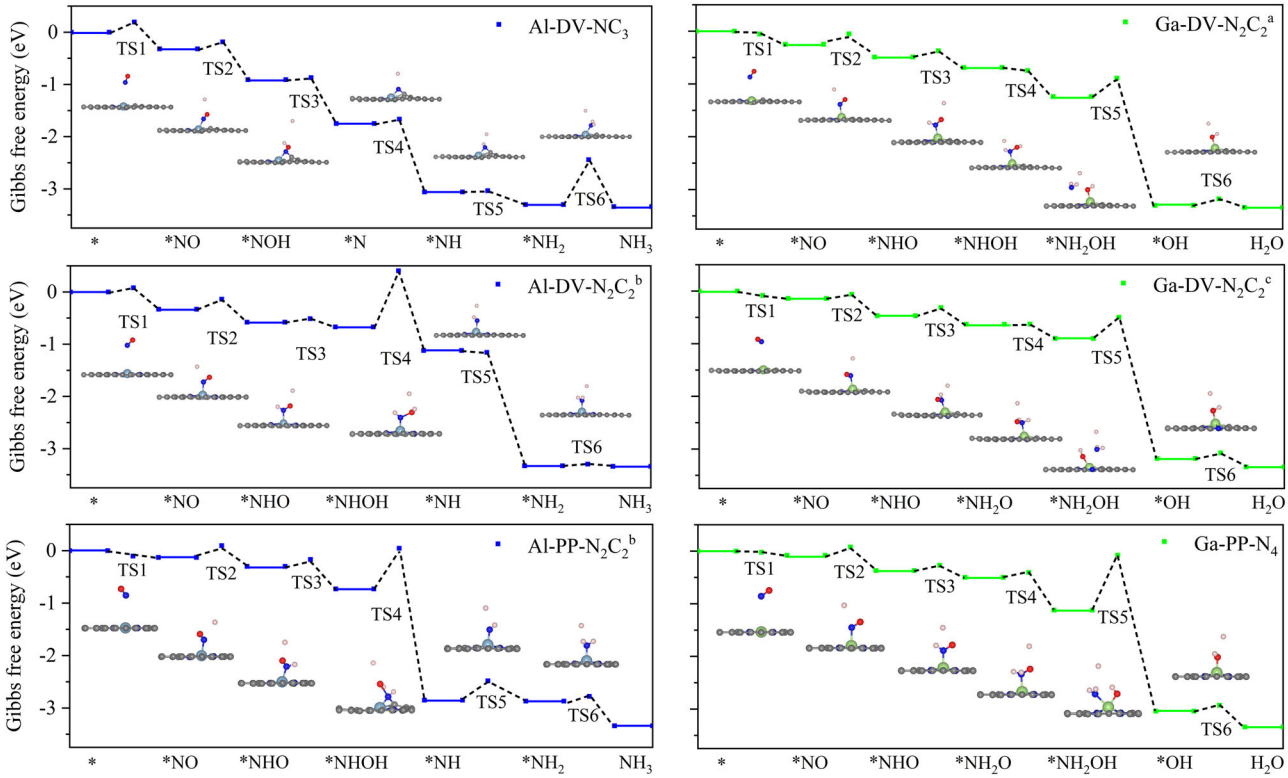


**Fig. 5 Kinetic barriers.** Corresponding kinetic barriers of the six screened SACs during the NORR toward $NH_3$ synthesis along the most thermodynamic favored reaction pathway. The insets are the structures of the transition states.

favored pathway for NORR to guarantee the excellent kinetic properties for these electrocatalysts. Therefore, we further calculate the kinetic barriers for each reaction step of the most thermodynamically favored pathway for Al-DV-$NC_3$, Al-DV-$N_2C_2$[b], Al-PP-$N_2C_2$[b], Ga-DV-$N_2C_2$[a], Ga-DV-$N_2C_2$[c], and Ga-PP-$N_4$. The corresponding transition states and kinetic barriers are presented in Fig. 5 and Supplementary Table 8. We can see that the hydrogenation of *$NH_2$ to $NH_3$(g) (TS6) is the rate-limiting step of Al-DV-$NC_3$ for the NORR, and the maximum kinetic barrier is 0.859 eV. The rate-limiting step is the hydrogenation of *NHOH to *NH + $H_2O$(l) (TS4) for both Al-DV-$N_2C_2$[b] and Al-PP-$N_2C_2$[b], and the maximum kinetic barriers are 1.076 eV and 0.775 eV, respectively. While for Ga-DV-$N_2C_2$[a], Ga-DV-$N_2C_2$[c], and Ga-PP-$N_4$, the rate-limiting step is the hydrogenation of *$NH_2$OH to *OH + $NH_3$(g), and the corresponding maximum kinetic barriers are 0.347 eV, 1.041 eV, and 0.401 eV, respectively. For Ga-DV-$N_2C_2$[a] and Ga-PP-$N_4$, the small activation barriers can be conquered at room temperature, so their NORR possess a high kinetic reaction rate. For the other four systems, although the activation barriers are relatively large, they can be easily conquered under the applied electrode potential[51–53].

To further understand the electrocatalytic performance of these six screened SACs for NORR, we simulate their electrochemical polarization curve using the microkinetic modeling analysis under the quasi-equilibrium approximation (the computational details are shown in "Methods"). The corresponding kinetic equations for all reaction steps of Al-DV-$NC_3$, Al-DV-$N_2C_2$[b], Al-PP-$N_2C_2$[b], Ga-DV-$N_2C_2$[a], Ga-DV-$N_2C_2$[c], and Ga-PP-$N_4$ are summarized in Supplementary Table 8. The calculated polarization curves of the screened six SACs during the NORR toward $NH_3$ are given in Supplementary Fig. 11. We can see that the polarization curve of Al-DV-$NC_3$, Al-DV-$N_2C_2$[b], Al-PP-$N_2C_2$[b], Ga-DV-$N_2C_2$[a], Ga-DV-$N_2C_2$[c], and Ga-PP-$N_4$ display an onset potential of −0.75 V, −1.30 V, −2.20 V, −1.15 V, −1.30 V, and −2.30 V, respectively. Therefore, Al-DV-$NC_3$ has the highest activity for NORR toward $NH_3$ synthesis.

In fact, recent works show that Li-atom-doped MgO exhibits high catalytic activity for oxidative coupling of methane reaction[54] and Pb single-atom catalyst exhibits good activity for combustion of energy materials[55]. Yet concerning SACs for NORR, the nonmetal and transition-metal atoms are exclusively active centers. Our work suggests that main group metal elements indeed can serve as compelling active centers of SACs for NORR, which has important guiding significance for NORR and SAC research. Furthermore, in contrast to previously reported metal bulk and TM-based electrocatalysts[31–35], these candidate structures display a potential-free NORR process. Moreover, they can avoid catalyst poisoning as they show a sizable $\Delta G_{*NO}$ (0~−1 eV vs. −2~−7 eV in competing systems[31,32,35,41]). We also calculate the turnover frequencies of these six screened SACs by using microkinetic modeling. The calculated turnover frequencies of these electrocatalysts for NORR toward $NH_3$ synthesis are much larger than the previously reported NRR toward $NH_3$ synthesis and the traditionally Harbor Bosch method toward $NH_3$ synthesis (Supplementary Table 9)[56,57]. Therefore, the six screened SACs exhibit superior thermodynamic and kinetic catalytic performance.

## Reaction mechanism of the main group metal SACs for NORR

Moreover, we investigate the reaction mechanism of the main group metal SACs for NORR. The relationship between the $\Delta G_{*NO}$ and NORR activity are summarized in Fig. 6a (for the candidates before the third screening step). It can be seen that there is a strong negative correlation between $\Delta G_{max\text{-}NH3}$ and $\Delta G_{*NO}$, suggesting $\Delta G_{*NO}$ as an excellent descriptor for NORR catalytic activity. By examining the partial density of states (PDOS) of the s/p-band for main-group metals shown in Supplementary Figs. 12–14, we find that $\Delta G_{*NO}$ is closely related to the s/p-band center ($\varepsilon_{s/p}$) of the main-group metal

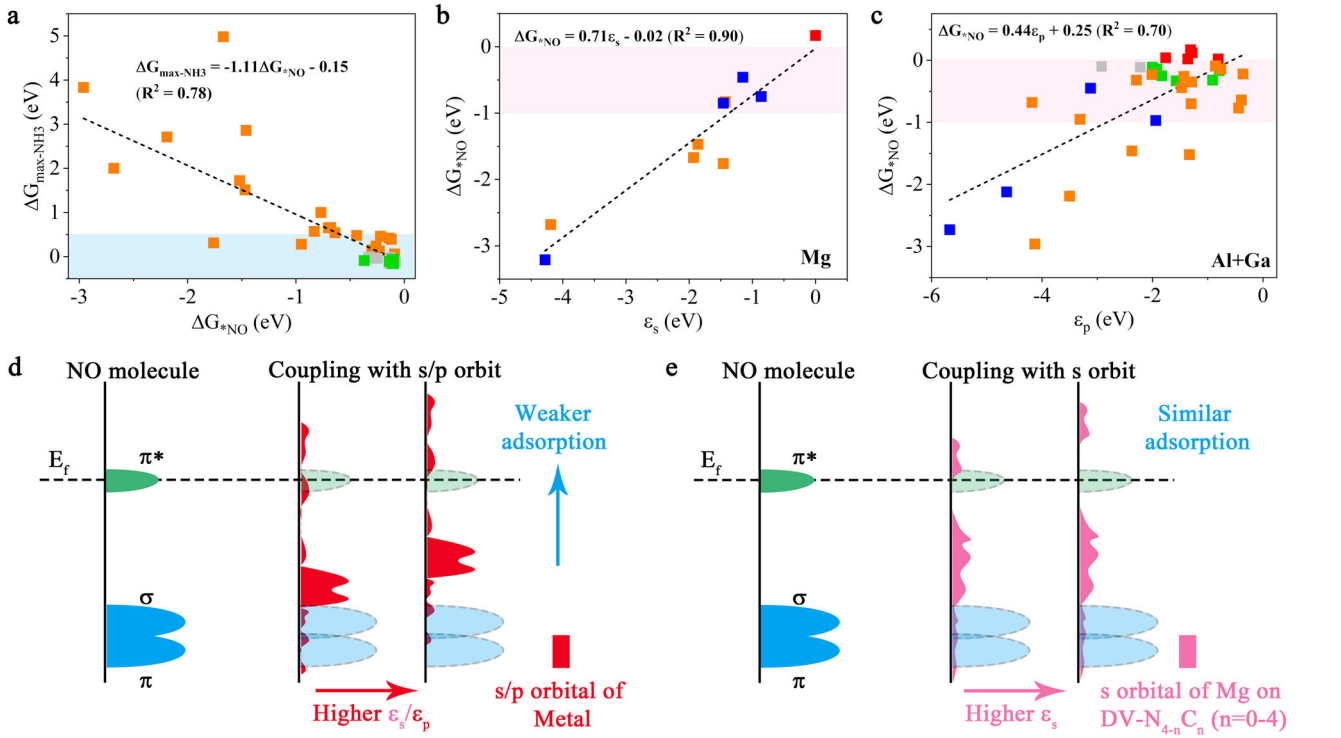


**Fig. 6 Descriptor and physical mechanism of catalytic activity. a** $\Delta G_{max\text{-}NH3}$ as a function of $\Delta G_{*NO}$. **b** $\Delta G_{*NO}$ as a function of s-band centers of Mg on SV/PP-related SAC candidates. **c** $\Delta G_{*NO}$ as a function of p-band centers of Al/Ga on SV/DV/PP-related SAC candidates. **d**, **e** Schematic illustrations of the interactions between NO molecular orbitals and s/p-band of main-group metals. The color code of (**a**–**c**) is consistent with Fig. 1d.

elements. The scaling relationships between $\varepsilon_{s/p}$ and $\Delta G_{*NO}$ for these 51 SAC candidates are illustrated in Supplementary Fig. 15. For the analysis of the valence electrons contributions, we distinguish between the outer s for Mg and p electrons for Al/Ga atoms, with their respective orbital energies $\varepsilon_s$ and $\varepsilon_p$. Intriguingly, for Al/Ga-related systems, there is a strong linear relation between $\Delta G_{*NO}$ and $\varepsilon_p$ (Fig. 6c). While for Mg-related systems, the relationship is a little complicated. In detail, $\Delta G_{*NO}$ is strongly correlated with $\varepsilon_s$ for Mg-SV-$N_{3-n}C_n$ and Mg-PP-$N_{4-n}C_n$ (Fig. 6b), while it is rather poor for Mg-DV-$N_{4-n}C_n$ (Supplementary Fig. 15b). The same is true for a correlation between $\Delta G_{*NO}$ and $\varepsilon_p$ for the same systems (Supplementary Figs. 15f, 16).

The interaction between NO and the SAC's main-group metals reveals deeper insight into their catalytic activity. According to orbital analysis, the bonding state of NO adsorption on main-group metal center originates from the hybridization between the σ molecular orbital of NO and s/p-band of Mg/Al/Ga. Shapes and relative positions of NO molecular orbitals are slightly affected by the adsorption for most of the systems, and the $\sigma$ orbital of NO mainly locates around −5 to −10 eV (Supplementary Figs. 17–20). While the s/p-band contribution of main-group metals is almost negligible as it lies within the range of −5 to −10 eV, the electrons of s/p-band of main-group metals, concentrated within 0 to −5 eV, are responsible to the binding strength of NO, as illustrated in Supplementary Figs. 12–14. Interestingly, we find that although the s/p-band of main group metals is generally delocalized[58], the s/p-band of metals within the energy range of 0 to −5 eV is relatively localized for Mg-SV-$N_{3-n}C_n$/-PP-$N_{4-n}C_n$ and Al/Ga-related systems. In this regard, as depicted in Fig. 6d, by varying the s/p-band center ($\varepsilon_{s/p}$), the hybridization between the σ molecular orbital and s/p-band upon adsorption will be changed, thus affecting the interaction as well as the activation strength. In detail, with a high(low)-lying $\varepsilon_{s/p}$ modulated by less (more) band filling, the coupling strength is weakened (enhanced), yielding a low (high) activity for NORR toward $NH_3$. Therefore, the high NORR activity can be readily achieved through tuning the $\varepsilon_{s/p}$ in these systems. We wish to emphasize that the position of $\varepsilon_{s/p}$ can be effectively modulated in such systems through engineering of the N-coordination environment. On the other hand, $\varepsilon_{s/p}$ is an intrinsic physical parameter that is relevant to the NORR activity. Because s/p-band center can be directly measured in experiment, it should arise the attention for designing main-group metal elements as active centers for NORR.

In contrast to the other systems, for Mg-DV-$N_{4-n}C_n$, the delocalized character of the Mg s-bands is well preserved (Supplementary Fig. 12), and thus the coupling between NO electrons and s-band of Mg cannot be regulated by $\varepsilon_s$. Such feature generally is prone to broaden the adsorbate states[22,24,25,59], yielding either too strong or too weak adsorption for adsorbates depending on the hybridization. But fortunately, the density of s-band is relatively low within the energy range of 0 to −5 eV (Supplementary Fig. 12), thus the interaction between the Mg and adsorbed NO is moderate with $\Delta G_{*NO}$ between 0 and −1 eV. With this result in hand, we understand why the $\varepsilon_s$ cannot define $\Delta G_{*NO}$ for Mg-DV-$N_{4-n}C_n$.

In summary, we comprehensively studied main-group metal elements as graphene-based active single-atom catalyst centers for direct NO-to-$NH_3$ conversion. By means of first-principles calculations, out of 51 candidates we identified six SAC systems with excellent catalytic activity and selectivity for NORR. For these SACs, the NORR process proceeds spontaneously without any limiting potential, and with moderate $\Delta G_{*NO}$ of 0 to −1 eV, which effectively avoids catalyst poisoning. Therefore, counter-intuitively, main-group metal elements indeed can serve as promising active centers for NORR SACs. We rationalize the excellent performance of these systems to the modulation of s/p-band filling of the main-group metal centers by regulating coordination environment. Our rational four-step screening principle is generally applicable for

exploring the possibility of introducing other main-group metals beyond Mg/Al/Ga to form SACs. We further discovered that the adsorption free energy of NO is an efficient catalytic descriptor for such SACs. The underlying physical mechanisms are revealed in detail. This work provides effective guidance for extending NORR SACs to main-group metal elements as well as for designing high-efficient NORR catalysts.

## METHODS

Spin-polarized first-principles calculations are performed using the Vienna ab initio simulation package (VASP)[60]. The projector augmented wave (PAW) method is used to describe the ion-electron interactions[61,62]. The exchange-correlation interactions are treated by the generalized gradient approximation (GGA) in form of Perdew-Burke-Ernzerhof (PBE) functional[63]. The plane-wave cutoff energy of 500 eV is adopted. To construct single (SV-$N_{3-n}C_n$, $n = 0$~3) and double (DV-$N_{4-n}C_n$, $n = 0$–4) vacancy systems, we substitute single and double carton atoms in the $4 \times 4 \times 1$ graphene supercells by single main group metal atom (Ma/Al/Ga), respectively. Brillouin zone is sampled using a Monkhorst-Pack grid of $3 \times 3 \times 1$. All structures are optimized with the convergence criteria of $10^{-5}$ eV and 0.01 eV $A^{-1}$ for energy and force, respectively. A vacuum space larger than 20 Å is employed to prevent adjacent interactions. Grimme's DFT-D3 correction is adopted to describe the van der Waals (vdW) interaction[64]. The corresponding optimized lattice parameters of the 51 SAC candidates are shown in Supplementary Table 1. The transition states and kinetic barriers are identified by the climbing image nudged elastic band (CI-NEB) method[65]. VASPKIT is adopted to obtain free energy correction[66]. Details on the Gibbs free energy calculations can be found in the Supplementary Method.

Microkinetic modeling is performed to simulate the electrochemical polarization curve. Under the quasi-equilibrium approximation[67,68], the reaction steps are all in equilibrium states except for the rate limiting step. $\theta_i$ and $P$ represent the coverage and pressure of reactants, respectively. The sum of coverage of all the reactants defines as $\Sigma\theta_i = 1$.

For NO adsorption step, the equilibrium constant ($K_i$), forward ($k_i$) and backward ($k_{-i}$) reaction rates are calculated by

$$K_i = e^{\frac{-G_i}{k_b T}} \tag{1}$$

$$k_i = \frac{k_b T}{h} e^{\frac{-\Delta G_{TS}}{k_b T}} \tag{2}$$

$$k_{-i} = \frac{k_i}{K_i} \tag{3}$$

where $G_i$, $G_{TS}$, $k_b$, $T$, and $h$ are the free energy change, kinetic barrier, Boltzmann constant, room temperature, and Planck constant, respectively.

For electrochemical reaction steps, the equilibrium constant ($K_i$), forward ($k_i$) and backward ($k_{-i}$) reaction rates are calculated by

$$K_i = e^{\frac{-e(U-G_i)}{k_b T}} \tag{4}$$

$$k_i = \frac{k_b T}{h} e^{\frac{-\Delta G_{TS}}{k_b T}} e^{\frac{-e\beta(U-G_i)}{k_b T}} \tag{5}$$

$$k_{-i} = \frac{k_i}{K_i} \tag{6}$$

where $U_i = -\Delta G_i/e$, $\beta = 1/2$, and $U$ is the applied electrode potential.

The turnover frequency (TOF) is calculated by solving the kinetic equations, and the current density ($j$) is obtained by $j = e\rho TOF$, where $e = 1.6 \times 10^6$ C, and ρ is the surface density of active sites.

The s/p-band center of MGMs is defined as

$$\varepsilon_{s/p} = \frac{\int_{-\infty}^{+\infty} E \times \rho_{s/p} dE}{\int_{-\infty}^{+\infty} \rho_{s/p} dE} \tag{7}$$

where $\rho_{s/p}$ is the density of s/p-band of main-group metals.

## DATA AVAILABILITY

The authors declare that the data supporting the findings of this study are available within the paper and its supplementary information files.

## CODE AVAILABILITY

The central code used in this paper is VASP. Detailed information related to the license and user guide is available at https://www.vasp.at.

Received: 10 March 2022; Accepted: 13 July 2022;
Published online: 01 August 2022

## REFERENCES

1. Qiao, B. et al. Single-atom catalysis of CO oxidation using $Pt_1/FeO_x$. *Nat. Chem.* **3**, 634 (2011).
2. Fu, Z., Yang, B. & Wu, R. Understanding the activity of single-atom catalysis from frontier orbitals. *Phys. Rev. Lett.* **125**, 156001 (2020).
3. Zhuo, H. Y. et al. Theoretical understandings of graphene-based metal single-atom catalysts: stability and catalytic performance. *Chem. Rev.* **120**, 12315 (2020).
4. Xu, H., Cheng, D., Cao, D. & Zeng, X. C. A universal principle for a rational design of single-atom electrocatalysts. *Nat. Catal.* **1**, 339 (2018).
5. Ling, C. et al. A general two-step strategy–based high-throughput screening of single atom catalysts for nitrogen fixation. *Small Methods* **3**, 1800376 (2019).
6. Wang, F. et al. Axial ligand effect on the stability of Fe–N–C electrocatalysts for acidic oxygen reduction reaction. *Nano Energy* **78**, 105128 (2020).
7. Tang, C. et al. Tailoring acidic oxygen reduction selectivity on single-atom catalysts via modification of first and second coordination spheres. *J. Am. Chem. Soc.* **143**, 7819 (2021).
8. Xue, Z., Zhang, X., Qin, J. & Liu, R. High-throughput identification of high activity and selectivity transition metal single-atom catalysts for nitrogen reduction. *Nano Energy* **80**, 105527 (2021).
9. Fu, Q. & Draxl, C. Hybrid organic-inorganic perovskites as promising substrates for Pt single-atom catalysts. *Phys. Rev. Lett.* **122**, 046101 (2019).
10. Sun, M., Dougherty, A. W., Huang, B., Li, Y. & Yan, C. H. Accelerating atomic catalyst discovery by theoretical calculations-machine learning strategy. *Adv. Energy Mater.* **10**, 1903949 (2020).
11. Tang, S. et al. Realizing a not-strong-not-weak polarization electric field in single-atom catalysts sandwiched by boron nitride and graphene sheets for efficient nitrogen fixation. *J. Am. Chem. Soc.* **142**, 19308 (2020).
12. Chen, Y. et al. Single-atom catalysts: synthetic strategies and electrochemical applications. *Joule* **2**, 1242 (2018).
13. Zhang, H., Liu, G., Shi, L. & Ye, J. Single-atom catalysts: emerging multifunctional materials in heterogeneous catalysis. *Adv. Energy Mater.* **8**, 1701343 (2018).
14. Wan, W. et al. Bifunctional single atom electrocatalysts: coordination–performance correlations and reaction pathways. *ACS Nano* **14**, 13279 (2020).
15. Yi, J. D. et al. Conductive two-dimensional phthalocyanine-based metal–organic framework nanosheets for efficient electroreduction of $CO_2$. *Angew. Chem. Int. Ed.* **133**, 17245 (2021).
16. Hannagan, R. T. et al. First-principles design of a single-atom–alloy propane dehydrogenation catalyst. *Science* **372**, 1444 (2021).
17. Wang, Y. et al. Elucidating the mechanism of the structure-dependent enzymatic activity of Fe–N/C oxidase mimics. *Chem. Commun.* **55**, 5271 (2019).
18. Cheng, G. & Perez-Mercader, J. Dissipative self-assembly of dynamic multi-compartmentalized microsystems with light-responsive behaviors. *Chem.* **6**, 1160 (2020).
19. Sun, M., Wong, H. H., Wu, T., Dougherty, A. W. & Huang, B. Stepping out of transition metals: activating the dual atomic catalyst through main group elements. *Adv. Energy Mater.* https://doi.org/10.1002/aenm.202101404 (2021).
20. Wu, Q. et al. Efficient nitric oxide reduction to ammonia on a metal-free electrocatalyst. *J. Mater. Chem. A* **9**, 5434 (2021).
21. Ling, C., Niu, X., Li, Q. & Du, A. J. Wang, Metal-free single atom catalyst for $N_2$ fixation driven by visible light. *J. Am. Chem. Soc.* **140**, 14161 (2018).
22. Légaré, M. A. et al. Nitrogen fixation and reduction at boron. *Science* **359**, 896 (2018).
23. Chen, J. et al. Demystifying the lattice oxygen redox in layered oxide cathode materials of lithium-ion batteries. *ACS Nano* **15**, 6061 (2021).
24. Hammer, B. & Nørskov, J. K. Theoretical surface science and catalysis-calculations and concepts. *Adv. Catal.* **45**, 71 (2000).
25. Zhu, B., Qiu, K., Shang, C. & Guo, Z. Naturally derived porous carbon with selective metal-and/or nitrogen-doping for efficient $CO_2$ capture and oxygen reduction. *J. Mater. Chem. A* **3**, 5212 (2015).
26. Cowan, J. A. Structural and catalytic chemistry of magnesium-dependent enzymes. *Biometals* **15**, 225 (2002).
27. Dunn, M. F., Ramírez-Trujillo, J. A. & Hernández-Lucas, I. Major roles of isocitrate lyase and malate synthase in bacterial and fungal pathogenesis. *Microbiology* **155**, 3166 (2009).
28. Sissi, C. & Palumbo, M. Effects of magnesium and related divalent metal ions in topoisomerase structure and function. *Nucleic Acids Res.* **37**, 702 (2009).

29. Yean, S.-L., Wuenschell, G., Termini, J. & Lin, R.-J. Metal-ion coordination by U6 small nuclear RNA contributes to catalysis in the spliceosome. *Nature* **408**, 881 (2000).
30. Long, J. et al. Direct electrochemical ammonia synthesis from nitric oxide. *Angew. Chem. Int. Ed.* **132**, 9798 (2020).
31. Xiao, Y. & Shen, C. Transition-metal borides (MBenes) as new high-efficiency catalysts for nitric oxide electroreduction to ammonia by a high-throughput approach. *Small* https://doi.org/10.1002/smll.202100776 (2021).
32. Niu, H. et al. A feasible strategy for identifying single-atom catalysts toward electrochemical NO-to-$NH_3$ conversion. *Small* https://doi.org/10.1002/smll.202102396 (2021).
33. Long, J. et al. Unveiling potential dependence in NO electroreduction to ammonia. *J. Phys. Chem. Lett.* **12**, 6988 (2021).
34. Koebel, M., Madia, G. & Elsener, M. Selective catalytic reduction of NO and $NO_2$ at low temperatures. *Catal. Today* **73**, 239 (2002).
35. Farberow, C. A., Dumesic, J. A. & Mavrikakis, M. Density functional theory calculations and analysis of reaction pathways for reduction of nitric oxide by hydrogen on Pt (111). *ACS Catal.* **4**, 3307 (2014).
36. Zhou, S. et al. Boron nitride nanotubes for ammonia synthesis: activation by filling transition metals. *J. Am. Chem. Soc.* **142**, 308 (2019).
37. Zhang, C. et al. Vanadium carbide with periodic anionic vacancies for effective electrocatalytic nitrogen reduction. *Mater. Today* **40**, 18 (2020).
38. Liu, X., Jiao, Y., Zheng, Y., Jaroniec, M. & Qiao, S. Z. Building up a picture of the electrocatalytic nitrogen reduction activity of transition metal single-atom catalysts. *J. Am. Chem. Soc.* **141**, 9664 (2019).
39. Guo, X. et al. Establishing a theoretical landscape for identifying basal plane active 2D metal borides (MBenes) toward nitrogen electroreduction. *Adv. Funct. Mater.* **31**, 2008056 (2021).
40. Peng, X. et al. Ambient electrosynthesis of ammonia with efficient denitration. *Nano Energy* **78**, 105321 (2020).
41. Niu, H. et al. Theoretical insights into the mechanism of selective nitrate-to-ammonia electroreduction on single-atom catalysts. *Adv. Funct. Mater.* **31**, 2008533 (2021).
42. Ha, M. et al. Tuning metal single atoms embedded in $N_xC_y$ moieties toward high-performance electrocatalysis. *Energ. Environ. Sci.* **14**, 3455 (2021).
43. Liu, S. et al. Turning main-group element magnesium into a highly active electrocatalyst for oxygen reduction reaction. *Nat. Commun.* **11**, 938 (2020).
44. Fei, H. et al. General synthesis and definitive structural identification of $MN_4C_4$ single-atom catalysts with tunable electrocatalytic activities. *Nat. Catal.* **1**, 63 (2018).
45. Luo, G., Jing, Y. & Li, Y. Rational design of dual-metal-site catalysts for electroreduction of carbon dioxide. *J. Mater. Chem. A* **8**, 15809 (2020).
46. Chen, B. et al. Engineering the active sites of graphene catalyst: from $CO_2$ activation to activate Li-$CO_2$ batteries. *ACS Nano* **15**, 9841 (2021).
47. Chang, Q. Y. et al. Rational design of single-atom-doped $Ga_2O_3$ catalysts for propane dehydrogenation: breaking through volcano plot by lewis acid–base interactions. *ACS Catal.* **11**, 5135 (2021).
48. Guo, W., Zhang, K., Liang, Z., Zou, R. & Xu, Q. Electrochemical nitrogen fixation and utilization: theories, advanced catalyst materials and system design. *Chem. Soc. Rev.* **48**, 5658 (2019).
49. Kaiser, S. K., Chen, Z., Faust Akl, D., Mitchell, S. & Pérez-Ramírez, J. Single-atom catalysts across the periodic table. *Chem. Rev.* **120**, 11703 (2020).
50. Wang, Z., Zhao, J., Wang, J., Cabrera, C. R. & Chen, Z. A Co–$N_4$ moiety embedded into graphene as an efficient single-atom-catalyst for NO electrochemical reduction: a computational study. *J. Mater. Chem. A* **6**, 7547 (2018).
51. Qian, J., An, Q., Fortunelli, A., Nielsen, R. J. & Goddard, W. A. Reaction mechanism and kinetics for ammonia synthesis on the Fe(111) surface. *J. Am. Chem. Soc.* **140**, 6288 (2018).
52. Logadóttir, Á. & Nørskov, J. K. Ammonia synthesis over a Ru(0001) surface studied by density functional calculations. *J. Catal.* **220**, 273 (2003).
53. Honkala, K. et al. Ammonia synthesis from first-principles calculations. *Science* **307**, 555 (2005).
54. Qian, K. et al. Single-site catalysis of Li-MgO catalysts for oxidative coupling of methane reaction. *ACS Catal.* **10**, 15142 (2020).
55. Qu, W. et al. Pb single atoms enable unprecedented catalytic behavior for the combustion of energetic materials. *Adv. Sci.* **8**, 2002889 (2021).
56. MacParland, S. A. et al. Single cell RNA sequencing of human liver reveals distinct intrahepatic macrophage populations. *Nat. Commun.* **9**, 1 (2018).
57. Chen, J. F., Mao, Y., Wang, H. F. & Hu, P. A simple method to locate the optimal adsorption energy for the best catalysts directly. *ACS Catal.* **6**, 7078 (2016).
58. Lundqvist, B. I., Gunnarsson, O., Hjelmberg, H. & Nørskov, J. K. Theoretical description of molecule-metal interaction and surface reactions. *Surf. Sci.* **89**, 196 (1979).
59. He, S. et al. The p-orbital delocalization of main-group metals to boost $CO_2$ electroreduction. *Angew. Chem. Int. Ed.* **130**, 16346 (2018).
60. Kresse, G. & Furthmuller, J. Efficient iterative schemes for Ab initio total-energy calculations using a plane-wave basis set. *Phys. Rev. B: Condens. Matter Mater. Phys.* **54**, 11169 (1996).
61. Blöchl, P. E. Projector augmented-wave method. *Phys. Rev. B: Condens. Matter Mater. Phys.* **50**, 17953 (1994).
62. Kresse, G. & Joubert, D. From ultrasoft pseudopotentials to the projector augmented-wave method. *Phys. Rev. B: Condens. Matter Mater. Phys.* **59**, 1758 (1999).
63. Perdew, J., Burke, K. & Ernzerhof, M. Generalized gradient approximation made simple. *Phys. Rev. Lett.* **77**, 3865 (1996).
64. Grimme, S. Semiempirical GGA-type density functional constructed with a long-range dispersion correction. *J. Comput. Chem.* **27**, 1787 (2006).
65. Henkelman, G., Uberuaga, B. P. & Jonsson, H. J. A climbing image nudged elastic band method for finding saddle points and minimum energy paths. *Chem. Phys.* **113**, 9901 (2000).
66. Wang, V., Xu, N., Liu, J., Tang, G. & Geng, W.-T. VASPKIT: a user-friendly interface facilitating high-throughput computing and analysis using VASP code. *Comput. Phys. Commun.* **267**, 108033 (2021).
67. Lynggaard, H., Andreasen, A., Stegelmann, C. & Stoltze, P. Analysis of simple kinetic models in heterogeneous catalysis. *Prog. Surf. Sci.* **77**, 71 (2004).
68. Stoltze, P. Microkinetic simulation of catalytic reactions. *Prog. Surf. Sci.* **65**, 65 (2000).

## ACKNOWLEDGEMENTS

This work is supported by the National Natural Science Foundation of China (Nos. 11804190, 12074217), Shandong Provincial Natural Science Foundation (Nos. ZR2019QA011 and ZR2019MEM013), Shandong Provincial Key Research and Development Program (Major Scientific and Technological Innovation Project) (No. 2019JZZY010302), Shandong Provincial Key Research and Development Program (No. 2019RKE27004), Shandong Provincial Science Foundation for Excellent Young Scholars (No. ZR2020YQ04), Qilu Young Scholar Program of Shandong University, and Taishan Scholar Program of Shandong Province. Deutsche Forschungsgemeinschaft is thanked for continuous support via CRC 1415, Shandong Provincial QingChuang Technology Support Plan (No. 2021KJ002).

## AUTHOR CONTRIBUTIONS

Q.W. executed calculations. Q.W., Y.M., and B.H. performed data analysis. Y.M., Y.D., and T.H. supervised the project. Q.W. and Y.M. co-wrote the paper. All authors discussed the results and commented on the manuscript at all stages.

## COMPETING INTERESTS

The authors declare no competing interests.

## ADDITIONAL INFORMATION

**Supplementary information** The online version contains supplementary material available at https://doi.org/10.1038/s41699-022-00326-4.

**Correspondence** and requests for materials should be addressed to Ying Dai, Thomas Heine or Yandong Ma.

**Reprints and permission information** is available at http://www.nature.com/reprints

**Publisher's note** Springer Nature remains neutral with regard to jurisdictional claims in published maps and institutional affiliations.